RESEARCH ARTICLE

Synthesis of calcium carbonate–loaded mesoporous SBA-15 nanocomposites for removal of phosphate from solution

Yaoyu Tang[1] · Hao Wang[1,2] · Wu Sun[1] · Dapeng Li[1] · Zhengying Wu[2] · Yifei Feng[3] · Nan Xu[1]

Abstract

Removal of phosphate from water is very crucial for protecting the ecological environment since massive phosphorus fertilizers have been widely used and caused serious water deterioration. Thus, we fabricated a series of calcium carbonate–loaded mesoporous SBA-15 nanocomposites with different Ca:Si molar ratio (CaAS-x) as phosphorus adsorbents via a simple wet-impregnation method. The multiply approaches including X-ray diffraction (XRD), N_2 physisorption, thermogravimetric mass spectrometry (TG-MS), X-ray photoelectron spectroscopy (XPS), and Fourier transform infrared (FT-IR) were used to characterize the structure, morphology, and composition of mesoporous CaAS-x nanocomposites. The phosphate adsorption efficiency of the CaAS-x nanocomposites was studied through adsorption and desorption batch tests. Results showed that the increases of Ca:Si molar ratio (rCa:Si) improved the phosphate removal capacity of CaAS nanocomposites, especially CaAS with the optimum synthesis molar ratio of Ca:Si as 0.55 showed the high adsorption capacity of 92.0 mg·g^{-1} to high concentration of phosphate (> 200 mg·L^{-1}). Note that the CaAS-0.55 had a fast exponentially increased adsorption capacity with increasing the phosphate concentration and correspondingly showed a much faster phosphate removal rate than pristine $CaCO_3$. Apparently, mesoporous structure of SBA-15 contributed to high disperse of $CaCO_3$ nanoparticles leading to the monolayer chemical adsorption complexation formation of phosphate calcium (i.e., =SPO_4Ca, =$CaHPO_4^-$, and =$CaPO_4Ca^0$). Therefore, mesoporous CaAS-0.55 nanocomposite is an environmental-friendly adsorbent for effective removal of high concentration of phosphate in neutral contaminated wastewater.

Keywords Calcium carbonate · SBA-15 nanocomposites · Phosphate · Adsorption; Removal

Introduction

In recent decades, environmental pollutions, especially water pollution, have drawn more and more attentions (Liu et al. 2012). Human activities and excessive use of fertilizer in agriculture has caused serious water eutrophication.

✉ Nan Xu
  nanxu@mail.usts.edu.cn

1   School of Environmental Science and Engineering, Suzhou University of Science and Technology, Suzhou 215009, China

2   Jiangsu Key Laboratory for Environment Functional Materials, School of Materials Science and Engineering, Suzhou University of Science and Technology, Suzhou 215009, China

3   School of Chemistry and Life Sciences, Suzhou University of Science and Technology, Suzhou 215009, China

Phosphorus (P) pollution includes municipal and industrial wastewater, agricultural drainage, stormwater runoff, and household sources, greatly threatens human and ecological health (Liu et al. 2013; Wen et al. 2014). This contamination has called on the requirements to develop the effective removal technologies or possible recovery of high concentration of phosphate from wastewater.

Various methods including ion exchange, biological removal, membrane separation, chemical precipitation, and adsorption have been widely developed to remove phosphate from surface water and ground water (Almanassra et al. 2020a; Wen et al. 2014). Among those techniques, adsorption is considered one of the most efficient technique due to its simple process, convenient operation, and excellent application for treating phosphate in wastewater (Almanassra et al. 2020; Mudhoo et al. 2019).

In the adsorption researches, finding effective adsorbents with high adsorption capacity is the key to facilitate the phosphate removal from wastewater. A bunch of work

has been done to design and develop the various absorbents, such as Fe and Fe oxides, Mg oxides, Al and Al oxides, soil minerals, and slag (Arslanolu 2021; Li et al. 2016). In recent years, calcite (calcium carbonate $CaCO_3$) as a natural mineral is regarded as a promising adsorbent for the removal of phosphate due to its abundant content, low cost, and environmental friendliness (Liu et al. 2012; Karageorgiou et al. 2007; Ramola et al. 2021). For example, a 10-mm-thick calcite capping layer has been applied to reduce 80% of the P efflux from sediment for at least 2–3 months (Berg et al. 2004). One gram of calcite can remove approximately 70–80% of phosphate in the solution under weak alkaline conditions (Yao et al. 2014). Nevertheless, the adsorption sites on $CaCO_3$ particles are not sufficient for effective phosphate adsorption due to its large particle size and small specific surface (Nath and Dutta 2010a, b; Qiu et al. 2021). Currently, some researches have been done to modify $CaCO_3$ by doping elements for improve their adsorption capacity of phosphate (Wang et al. 2021). However, the limited information is available in $CaCO_3$ nanosized and distributed in a porous support to increase the specific surface area.

As known, the ordered mesoporous material SBA-15 has been commonly used as a good support for the preparation of catalysts, due to its open structure, high surface area, large pore diameter, thick pore walls, and good hydrothermal stability (Wu et al. 2014). Likewise, nanomaterials have great chemical activity and surface energy, which could be easily combined with supports through the surface hydroxyl reaction (Zhou et al. 2011). Obviously, nanomaterials loaded onto the SBA-15 support could show great potential for preparation of composites with the high-performance of application in pollutant removal. For example, nanoparticles (i.e., metal oxides (Wu et al. 2014; Wu et al. 2018), MOFs (Mahmoudi et al. 2020), Ag_3PO_4 (Chai et al. 2015), spinel $NiFe_2O_4$ (Chen et al. 2017), and so on) have been loaded on SBA-15 to fabricate the nanocomposites for removal of organic pollutants from water. Besides, loading the metal nanoparticles onto SBA-15 to form nanocomposites has been used for removal of heavy metals from water. For example, nanoscale zero-valent iron (nZVI) composites by loading into polydopamine (PDA)-decorated SBA-15 exhibited the excellent removal capacity of Cr(VI) and U(VI) from aqueous solutions (Liu et al. 2021a, b). Moreover, the SBA-15@Fe/Ni composite, prepared via loading nZVI onto SBA-15 as a support, showed the enhanced stability and removal capacity for Cr(VI) adsorption and reduction (Xing et al. 2023). However, the synthesis and application of SBA-15-based nanocomposites in the phosphate removal from wastewater are rarely investigated.

In this study, the porous $CaCO_3$-loaded SBA-15 nanocomposites (CaAS) were successfully prepared by a simple wet-impregnation method to effective remove high concentration of phosphate from water. Then, a series of CaAS composites with different loading ratios were characterized. The adsorption and desorption of phosphate on an idealist composite CaAS were investigated. Particularly, the underlying mechanisms for chemical reactions between CaAS composite and phosphate were unraveled by multiple characterization including thermogravimetric analysis (TGA), powder X-ray diffraction (XRD), and Fourier transform infrared (FT-IR).

Materials and methods

Chemicals

Triblock copolymer P123 (polyoxyethylene-polyoxypropylene-polyoxyethylene, EO20PO70EO20, $M_W = 5800$), Sigma-Aldrich; hydrochloric acid (HCl, 35–37 wt%); calcium acetate (calcium acetate); and tetraethyl orthosilicate (TEOS) were purchased from Sinopharm Chemical Reagent Co. Ltd. of China. These chemicals were analytically pure and used without further purification. Deionized water was used in the experiments.

Materials synthesis

Mesoporous SBA-15 was synthesized through a hydrothermal method (Xu et al. 2014). Typically, 0.5 g of SBA-15 and a certain amount of calcium acetate monohydrate ($Ca(CH_3OO)_2·H_2O$, 99.8%) were mixed with water to ensure the different Ca/Si molar ratio (rCa/Si) for the synthesis of CaAS-x ($x = 0.1–0.6$) nanocomposites. The mixture was then dried by distillation after stirring at room temperature for 24 h, then heated at 50 °C. Finally, the powder was calcined in a muffle furnace with 500 °C for 2 h to obtain the final product.

Material characterization

X-ray diffraction (XRD, Bruker D8 Advanced, Germany) was performed to characterize the structure of the synthesized materials. Thermogravimetric (TG, NETZSCH STA449F3, Germany) and mass spectrometry (MS, Agilent 7890B-7200, USA) analyses were performed on a thermo balance (SDQ-600) with a heating rate of 20 °C/min up to 800 °C under air flow. Fourier transform infrared (FT-IR, Nicolet iS10, Thermo Fisher Scientific, USA) spectra were performed on an IRPrestige-21 Fourier infrared spectrometer with KBr wafer. X-ray photoelectron spectroscopy (XPS) measurements were analyzed by Thermo Fisher Scientific ESCALAB 250.

Batch experiments

Phosphate adsorption tests onto different Ca/Si molar ratio of CaAS-*x* were conducted to investigate the ideal synthesis ratio of Ca/Si for CaAS nanocomposites. CaAS-*x* series (5.0 g·L^{-1}) were mixed with 200 and 500 mg·L^{-1} phosphate solutions at 25 °C room temperature. Solutions were centrifuged for 10 min using the RJ-TDL-40B low-speed desktop centrifuge, and then passed through a 0.45-mm pore filter. Finally, the molybdenum blue colorimetric method using UV-vis spectrophotometry (UV-2450, Shimadzu, Japan) was employed to determine the phosphate concentration in the filtrate based on pre-established phosphate calibration curves.

Phosphate adsorption kinetics were initially obtained to acquire best reaction time. The 1.0-g·L^{-1} of CaAS-0.55, CaCO$_3$, and SBA-15 materials were added into 100 mg·L^{-1} phosphate solution which was diluted with sodium dihydrogen phosphate stock solution of 1000 mg·L^{-1} in 10 mM NaCl solution, respectively. After that, mixtures were filled in many 50 mL centrifuge tubes and transferred on rotators for varying reaction time (0.1–18 h). The phosphate adsorption capacity was defined as the phosphate adsorption amount (difference between initial and equilibrium phosphate concentrations in solution) per gram of material, which agreed with previous study (Xu et al. 2014a, b).

Adsorption isotherms were obtained by adding CaAS-0.55, CaCO$_3$, or SBA-15 (1.0 g·L^{-1}) into different concentrated phosphate solutions (5−250 mg·L^{-1}) at 20 °C for reaction 18 h. Meanwhile, pH effect on phosphate adsorption capacity of materials was also investigated under similar experimental conditions.

Desorption kinetic experiment

At first, 200 mM phosphate was pre-adsorbed onto CaAS-0.55 by equilibrating 5 g·L^{-1} of absorbent in 10 mM NaCl solution at pH 7.0. And then, supernatant was discarded and refilled with NaCl solution. After being subjected to 1–14 days equilibrium period, the solids were centrifuged and then filtered through a 0.45-μm filter. The desorption efficiency was calculated as the percentage of phosphate in filtrate versus phosphate pre-adsorbed on absorbent.

Theoretical analysis and modeling

The adsorption kinetic curves were fitted by pseudo-first-order and pseudo-second-order models (Wu et al. 2014), as follows:

Pseudo-first-order equation:

$$Q_t = Q_e \times \left(1 - e^{-k_1 t}\right) \tag{1}$$

Pseudo-second-order equation:

$$t/Q_t = 1/k_2 Q_e^2 + t/Q_e \tag{2}$$

where Q_t (mg·g^{-1}) and Q_e (mg·g^{-1}) are the amounts adsorbed at predetermined and equilibrium adsorption time, respectively; t (h) represents contact time; k_1 (h^{-1}) and k_2 (g·mg^{-1}·h^{-1}) are the rate constants of the pseudo-first-order and pseudo-second-order models, respectively.

The phosphate adsorption mechanisms by adsorbents were explained by Langmuir and Freundlich adsorption models, as following equations (Wang et al. 2022a, b):

Langmuir model

$$Q_e = \frac{Q_{max}K_L C_e}{1 + K_L C_e} \tag{3}$$

Freundlich model

$$Q_e = K_F C_e^{1/n_F} \tag{4}$$

C_e (mg·L^{-1}) in the equations is the equilibrium concentration of phosphate solution; Q_e (mg·g^{-1}) is the adsorbed amount per gram of material at adsorption equilibrium; Q_{max} (mg·g^{-1}) is the largest amounts of monolayer adsorption; K_L (L^{-1}·mg) is the Langmuir constant; K_F ([mg·g^{-1}·(L·mg^{-1})$^{1/n}$]), and $1/n_F$ are the Freundlich constants, which are the adsorption capacity and adsorption intensity, respectively.

Results and discussion

Material characterizations

Figure 1 a shows the low angle XRD patterns of CaAS-*x* samples with different Ca/Si molar ratio. There were three apparent feature peaks with 0.92, 1.58, and 1.82 degrees of 2theta for all samples, which corresponded to the diffraction peaks of (100), (110), and (200), respectively, of the hexagonal symmetrical structure (space group: p6mm) (Gu et al. 2019). It was revealed that all samples have highly ordered mesoporous structure as the SBA-15 support after loading CaCO$_3$. With the increase of CaCO$_3$ loading number, the XRD diffraction peak shifted to low angle. If the Ca/Si molar ratio of the sample was changed from 0.1/1 to 0.5/1, the (100) peak in corresponding samples changes from 2theta of 0.94 to 0.88°, which indicated that the lattice parameter of SBA-15 further increased after modification by CaCO$_3$. When the loaded CaCO$_3$ was further increased to Ca/Si molar ratio = 0.55 and 0.6, the XRD diffraction peak of the samples shifted to high angle. The (100) peak of the CaAS-0.55 and CaAS-0.6 samples is at 0.92°, which revealed that the lattice parameter of the sample would not change along with the higher CaCO$_3$ loading.

Figure 1 b presents the wide-angle XRD patterns of CaAS-*x* samples. Distinct diffraction peaks at 23.1°, 29.3°,

Fig. 1 Low (**a**) and wide (**b**) XRD patterns of CaAS-*x* (*x* = 0.1−0.6) samples with different Ca/Si molar ratio
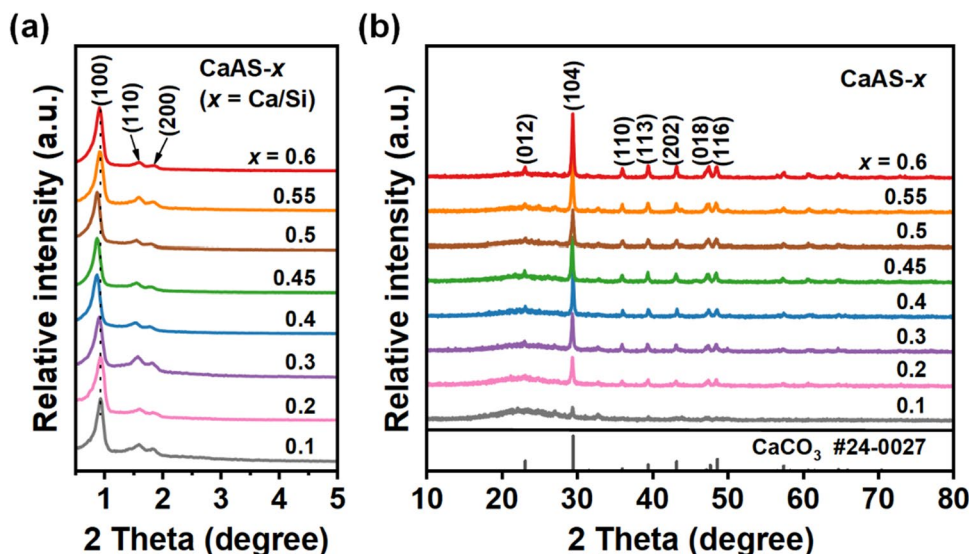
36.0°, 39.5°, 43.2°, 47.4°, and 48.5°, corresponding to the (012), (104), (110), (113), (202), (018), and (116) planes of $CaCO_3$ (JCPDS card no. 24-0027) were observed for the CaAS-*x* samples (Gu et al. 2022). Moreover, intensity of the diffraction peaks gradually raised following by the increase in the *r*Ca/Si. Furthermore, a broad peak around 22.5° appeared in the samples with relatively lower $CaCO_3$ content (*r*Ca/Si = 0.1~0.45), which corresponds to amorphous SiO_2. Intensity of this peak decreased along with the increase in $CaCO_3$ content due to reduce of relative content of mesoporous SiO_2. No XRD diffraction peaks according to other crystal phases appeared in the XRD patterns, indicating there is no impurities in the CaAS-*x* samples (Fig. 1b).

Figure 2 shows the N_2 adsorption/desorption isotherms and corresponding pore size distributions (PSDs) of the CaAS-*x* materials. All of the CaAS-*x* samples with different *r*Ca/Si displayed type IV sorption isotherms with type H1 hysteresis loops at high relative pressures (Fig. 2a, c), indicating characteristic mesoporous channels of SBA-15 were maintained after the modification by $CaCO_3$ (Wu et al. 2014). Moreover, the N_2 adsorption amount of the CaAS-*x* decreased along with the increase in $CaCO_3$ loading number, which is due to the fact that $CaCO_3$ would occupy partial pores of the mesoporous support. Consequently, the BET surface area and pore volume of CaAS-*x* samples gradually declined from 289 to 148 $m^2 \cdot g^{-1}$ when the *r*Ca/Si raises from 0.1 to 0.6 (Table 1).

The PSD curves of the CaAS-*x* revealed that all materials have narrow pore size distributions, confirming the uniform mesopores in them (Fig. 2b, d). The CaAS-*x* materials with different *r*Ca/Si had relatively large surface areas of 289–148 $m^2 \cdot g^{-1}$ and pore volumes of 0.52–0.28 $cm^3 \cdot g^{-1}$, respectively, which are lower than those of the SBA-15 support (Table 1).

Figure 3 gives TG and DSC results of $Ca(CH_3COO)_2 \cdot H_2O$ and as-synthesized CaAS-0.2 samples. The

$Ca(CH_3COO)_2 \cdot H_2O$ had obvious weight loss at 80–220 °C; the percentage of weight loss was about 8%, which corresponded to desorption of adsorbed water and molecular water (Fig. 3a). The DSC heat flow signal corresponded to a less apparent endothermic peak, as shown in Fig. 2b. The first part of the thermal decomposition of calcium acetate samples occurred at 400–450 °C; the weight loss ratio was about 33%. The weight loss of this section should be the decomposition of calcium acetate to produce acetone and calcium carbonate. The second apparent weight loss interval of calcium acetate in air atmosphere was in the range of 630–760 °C, corresponding to the decomposition of calcium carbonate. DSC signal displayed that there was apparent endothermic peak around 750 °C.

Figure 3 shows that the thermal decomposition temperature of CaAS-0.2 ($CaCO_3$-loaed SBA-15) was close to that of calcium acetate. When the temperature was 470 °C, calcium acetate decomposed completely. Compared with calcium acetate, the initial decomposition temperature of CaAS-0.2 sample advanced and the weight loss rate was relatively flat after combining with SBA-15. Samples were slowly decomposed from 200 to 400 °C of which the first part of the decomposition was completed. Meanwhile, the loaded calcium acetate was completely converted to calcium carbonate when temperature increased further to 470 °C; the calcination temperature of loaded sample was selected as 500 °C. In addition, the phenomenon of decomposition of calcium oxide and CO_2 in high temperature region by CaAS-0.2 ($CaCO_3$-loaded SBA-15) was less transparent than pure calcium acetate, which may be due to the interaction between SBA-15 and Ca species.

Figure 4 displays the MS curve of carbon dioxide and acetone during the thermal degradation of $Ca(CH_3COO)_2 \cdot H_2O$. The results showed the decomposition mechanism of calcium acetate. With the increase of temperature, MS signals

Fig. 2 N$_2$ adsorption/desorption isotherms (**a** and **b**) and pore size distribution curves (**c** and **d**) of the mesoporous CaAS-*x* (*x* = 0.1−0.6) samples synthesized with different Ca/Si molar ratio
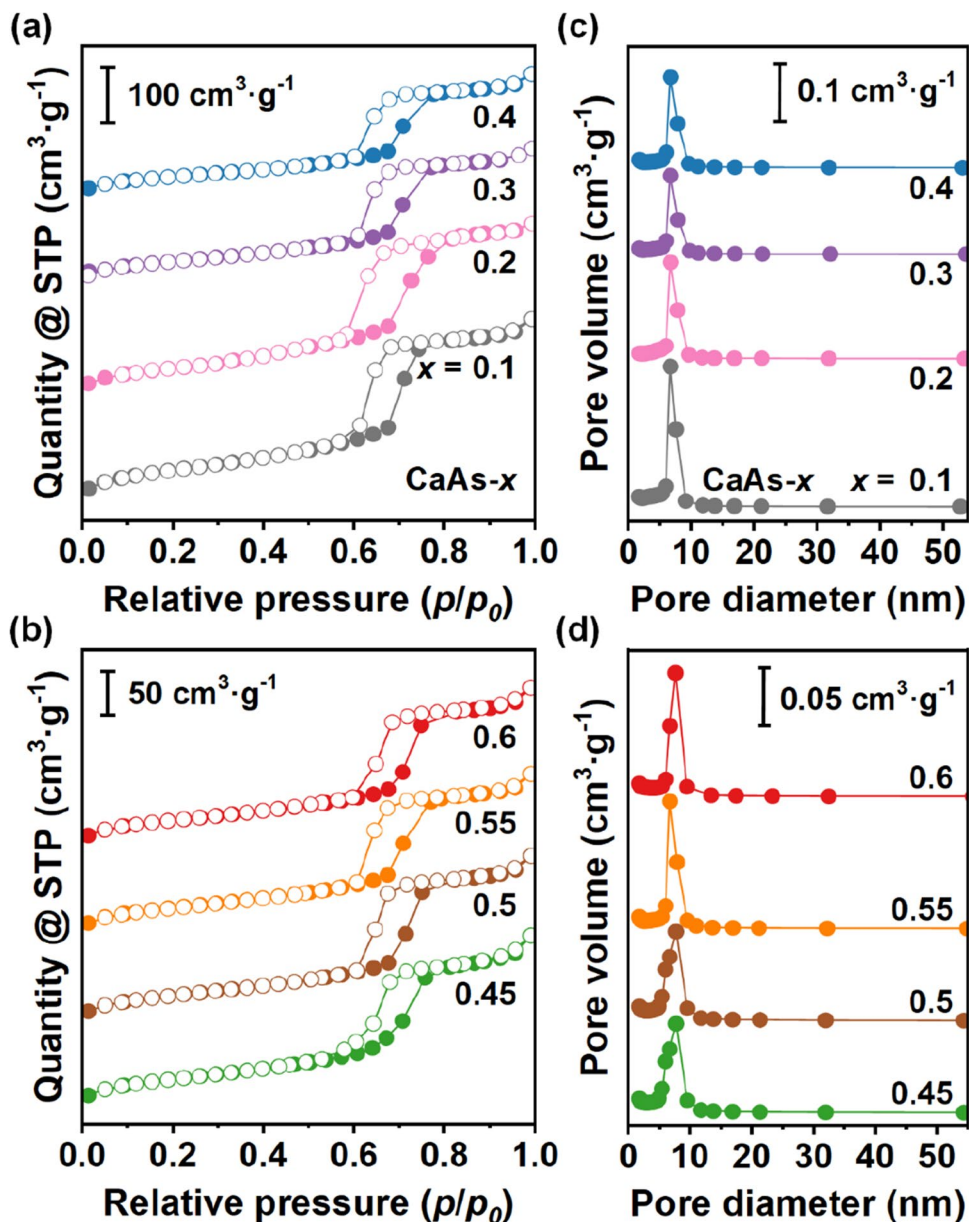
Table 1 Textural properties of the mesoporous CaAS-*x* materials

Samples	S_{BET} (m^2·g^{-1})	V_p (cm^3·g^{-1})	D_p (nm)
CaAs-0.1	289	0.52	7.24
CaAs-0.2	254	0.44	6.98
CaAs-0.3	216	0.40	7.24
CaAs-0.4	183	0.35	7.67
CaAs-0.45	161	0.31	7.60
CaAs-0.5	158	0.30	7.58
CaAs-0.55	151	0.29	7.58
CaAs-0.6	148	0.28	7.64

of acetone and carbon dioxide could be clearly observed. During the thermal treatment, calcium acetate was firstly decomposed to produce calcium carbonate and acetone, following with a part of acetone convert to carbon dioxide. Then, calcium carbonate was further decomposed into calcium oxide and carbon dioxide. The temperature in the decomposition process was vital and should be controlled at about 500 °C. At 500 °C, calcium acetate was completely decomposed but not form calcium oxide.

Figure 5 is FT-IR spectra of SBA-15 and CaAS-*x* samples synthesized with different *r*Ca/Si. The characteristic peak of about 960 cm^{-1} corresponded to silanol groups (=Si-OH)
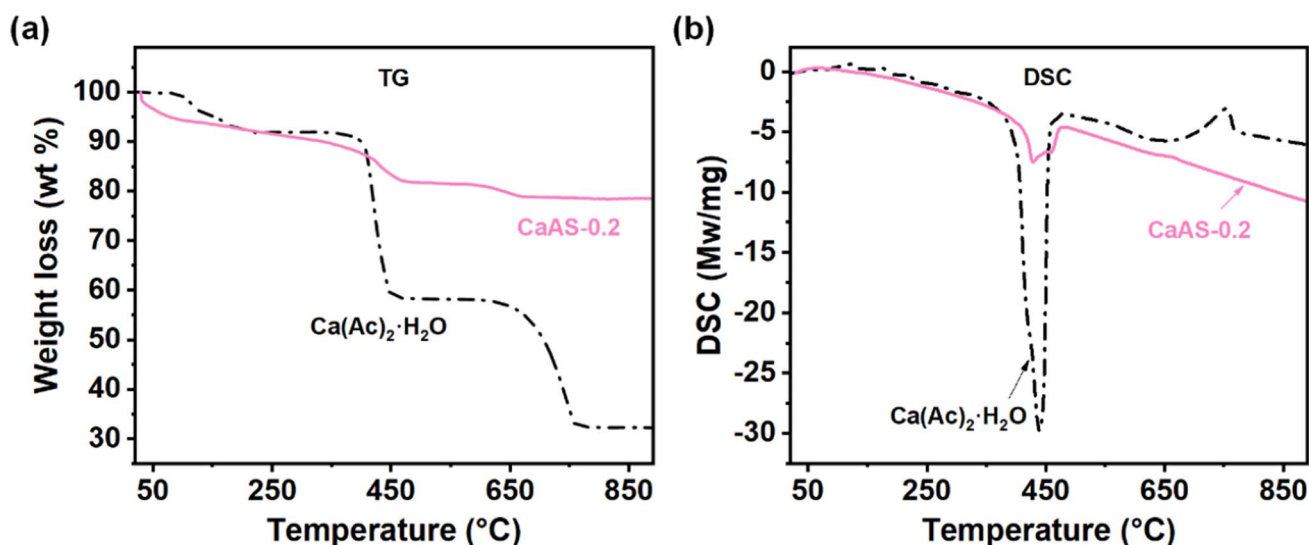
Fig. 3 TG (**a**) and DSC (**b**) results of $Ca(CH_3COO)_2 \cdot H_2O$ and synthesized CaAS-0.2 samples

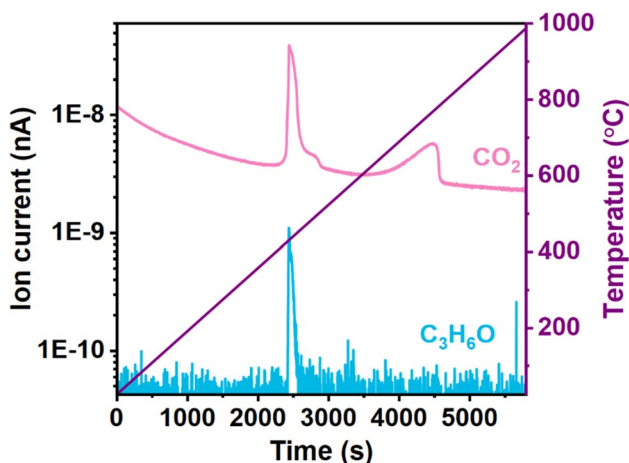**Fig. 4** MS curves of CO_2 and acetone during the degradation of $Ca(CH_3COO)_2 \cdot H_2O$

on the surface of SBA-15. The characteristic peak at 960 cm^{-1} was gradually weakened with the increase of $CaCO_3$ loading. When the rCa/Si = 0.4, the absorption peak at 960 cm^{-1} for CaAS-0.4 was deteriorated to be an acromion. Further increase the $CaCO_3$ loading amount, this weak absorption peak did not change or disappear, which indicated the strong interactions between Ca and Si species. At the same time, the absorption bands at 462, 802, and 1079 cm^{-1} that correspond to Si−O−Si bending vibration [δ(Si−O−Si)], symmetric stretching vibration [v_s(Si−O−Si)], and anti-symmetric stretching vibration [v_{as}(Si−O−Si)] did not change (Fig. 5) (Zhang et al. 2022), indicating that the siliceous framework of SBA-15 was maintained after the modification by $CaCO_3$. Compared with SBA-15, new infrared peaks at 1431, 874, and 713 cm^{-1} assigned to C–O asymmetric

stretching vibrations of carbonate (Ramola et al. 2021; Taweekarn et al. 2022) appeared in the CaAS-x samples (Fig. 5). As the content of Ca/Si ratio increased from 0.1 to 0.4 in $CaCO_3$, the intensity of the absorption peak improved gradually (Fig. 5a). Further increasing the rCa/Si ratio to 0.45–0.6, intensity of the absorption peak of $CaCO_3$ changed no longer evidently (Fig. 5b).

Phosphate adsorption on different CaAS-x nanocomposites

Phosphate adsorption onto porous CaAS-x nanocomposites with increasing the Ca/Si molar ratio from 0.1 to 0.6 was investigated in NaCl background solution, in order to determine the optimum synthesis ratio of Ca/Si (Fig. 6). The sorption sites on absorbent (T, mg·L^{-1}), which is defined as the uptake maximum (mg·g^{-1}) multiplied with the adsorbent mass concentration (g·L^{-1}) (Ramola et al. 2021), were used in this study to better compare and describe uptake capacity. As expected, a clear improvement in phosphate uptake at equilibrium was observed for CaAS-x with the increase of Ca/Si molar ratio. For instance, the phosphate uptake amount remarkably improved from 21.2 mg·g^{-1} (53%, T = 106 mg L^{-1}) to 38.4 mg·g^{-1} (96%, T = 192 mg·L^{-1}) for CaAS-0.1 and CaAS-0.3 in 200 mg·L^{-1} P solution at pH 7.0, respectively (Fig. 6). It probably ascribed to the increase of the adsorption sites and surface precipitation promoted by the enhanced Ca species incorporation (House and Denison 2000; Klibanski et al. 2007). Nevertheless, the more introduction of $CaCO_3$ (Ca/Si > 0.3) showed negligible influence in uptake capacity of material. For example, as shown in Fig. 6, uptake capacities for CaAs-0.4 and CaAs-0.6
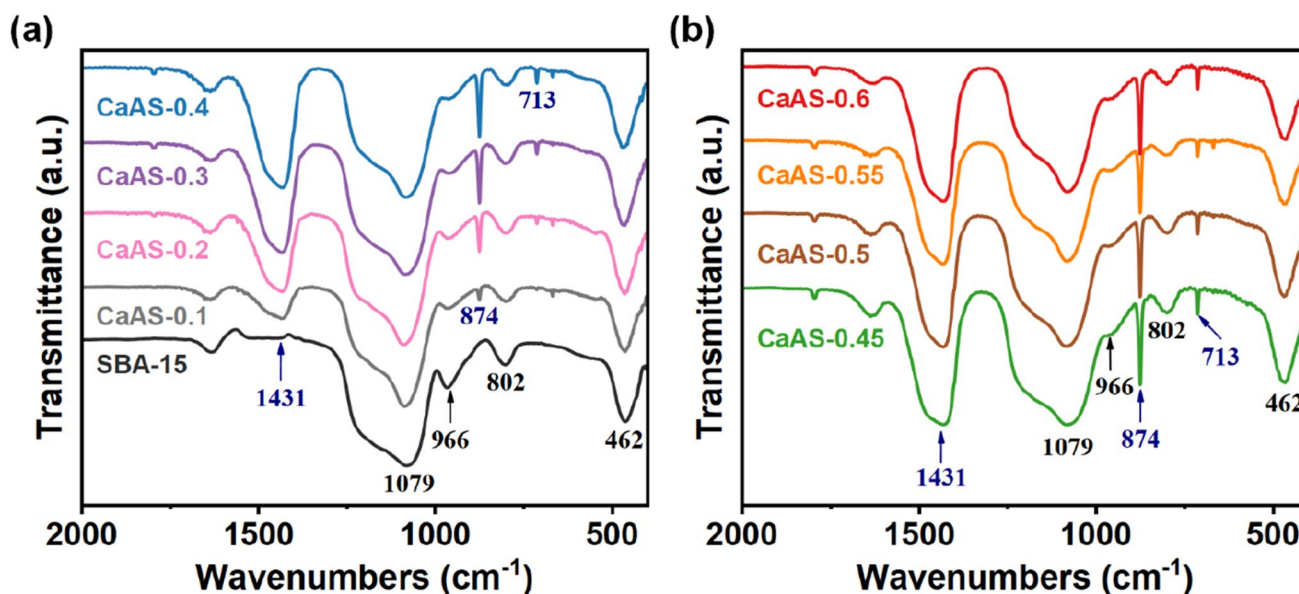
Fig. 5 FT-IR spectra of SBA-15 and CaAS-*x* (*x* = 0.1−0.6) samples synthesized with different Ca/Si molar ratio
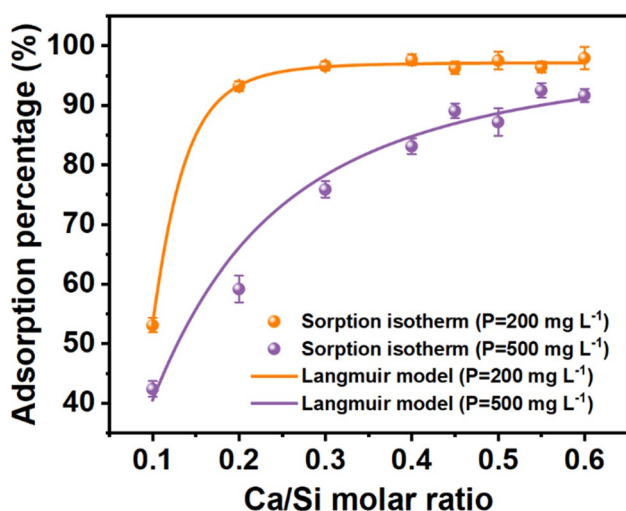

Fig. 6 Phosphate adsorption (200 and 500 mg L^{-1}) onto synthesized CaAS-*x* nanomaterials as a function of Ca/Si molar ratio

were 39.2 mg·g^{-1} (98%, T = 196 mg·L^{-1}) and 39.6 mg·g^{-1} (99%, T = 198 mg·L^{-1}), respectively. Therefore, the introduction of CaCO$_3$ on SBA-15 material played a crucial role to improve phosphate uptake. The estimated maximum T for CaAs-*x* was ~ 198 mg·L^{-1} for 200 mg·L^{-1} phosphate adsorption at pH 7.0, when Ca/Si molar ratio was greater than 0.3. The adsorption experiments revealed that 200 mg·L^{-1} of P can be efficiently absorbed by the synthesized CaAS-*x* (*x* ≥ 0.3) at pH 7.0 (Fig. 6). In another words, the optimum Ca/Si ratio for synthesized CaAS-*x*

needs to be greater than 0.3 for efficient removal of phosphate (>200 mg·L^{-1}).

To further reveal the relation between the Ca/Si molar ratio of CaAS-*x* nanocomposites and the corresponding removal capacity to phosphate, the higher concentration of phosphate (500 mg·L^{-1}) was also addressed for comparison in a systematic fashion (Fig. 6). It was found that CaAS-*x* had a similar increase of removal efficiency to higher phosphate with the increase in Ca/Si molar ratio from 0.1 to 0.55 (Fig. 6). For instance, CaAS-0.55 (Ca/Si = 0.55) had a high removal efficiency of 92 mg·g^{-1} (92%, T = 460 mg·L^{-1}), while CaAS-0.1 with Ca/Si molar ratio of 0.1 had a lowest removal capacity of 42 mg·g^{-1} (42%, T = 210 mg·L^{-1}). It was agreed with the increase of phosphate uptake with increasing Ca species incorporation in synthesized material (Vohla et al. 2011). The maximum phosphate adsorption efficiency of CaAS-0.55 might be attributed to the maximum introduction of CaCO$_3$ in mesoporous SBA-15 without increasing SiO$_2$ lattice parameters as shown in Fig. 1. This result was consistent with previous study that the effective removal of strontium by manganese dioxide–loaded SBA-15 (Dan et al. 2020). Note that phosphate adsorption improved with increasing initial phosphate concentration (Fig. 6). For instance, CaAS-0.55 showed the uptake of 38.8 mg·g^{-1} and 92.0 mg·g^{-1} to 200 and 500 mg L^{-1} phosphate (Fig. 6), respectively. This was consistent with previous study (Moharami and Jalali 2013). Herein, CaAS-*x* with Ca/Si > 0.5 was ideal adsorbent for high phosphate removal from wastewater at pH 7.0. The maximum phosphate uptake by CaAs-0.55/0.6 (92.0 mg·g^{-1}) was obviously stronger than that of most artificial materials and natural adsorbents (Xu

et al. 2014). For example, the sorption capacities of kaolinite (natural adsorbents), zeolite, and mesoporous MgO microspheres (artifact) were 0.28–0.32 (Peen and Warren 2009), 41.17 (Chen et al. 2006), and 3.1–75.1 mg·g^{-1} (Zhou et al. 2011), respectively. Noted that the phosphate adsorption capacity of CaAS-*x* nanocomposites was primarily dependent on the CaCO$_3$ content, not BET surface area (S_{BET}) of the adsorbent, since S_{BET} of CaAS-*x* samples decreased with increasing the Ca:Si ratio, while the phosphate adsorption capacity of CaAS-*x* samples improved (Table 1; Fig. 6).

Phosphate adsorption kinetics of CaAS-0.55 material

Figure 7 a shows the phosphate adsorption kinetics of CaAS-0.55, pristine CaCO$_3$, and mesoporous SBA-15 materials. The phosphate adsorption capacity of CaAS-0.55

nanocomposite initially raised up fast in first 4 h and then gradually reached equilibrium after 6 h (Fig. 7a). For example, CaAS-0.55 had a 58.8 mg·g^{-1} of phosphate adsorption capacity. In contrast, pristine CaCO$_3$ displayed a relatively lower uptake about 5.1 mg·g^{-1} in first 2 h, which was similar to that (3.7 mg·g^{-1}) of SBA-15. The phosphate uptake by CaCO$_3$ slowly increased until achieving the adsorption equilibrium at 18 h (Fig. 7a). Overall, CaAS-0.55 showed the much stronger phosphate removal ability than pristine CaCO$_3$ and mesoporous SBA-15.

Phosphate adsorption isotherms of CaAS-0.55 material

In order to quantify the maximum phosphate adsorption capacity, the phosphate adsorption isotherms of the optimized material (CaAS-0.55), mesoporous SBA-15, and
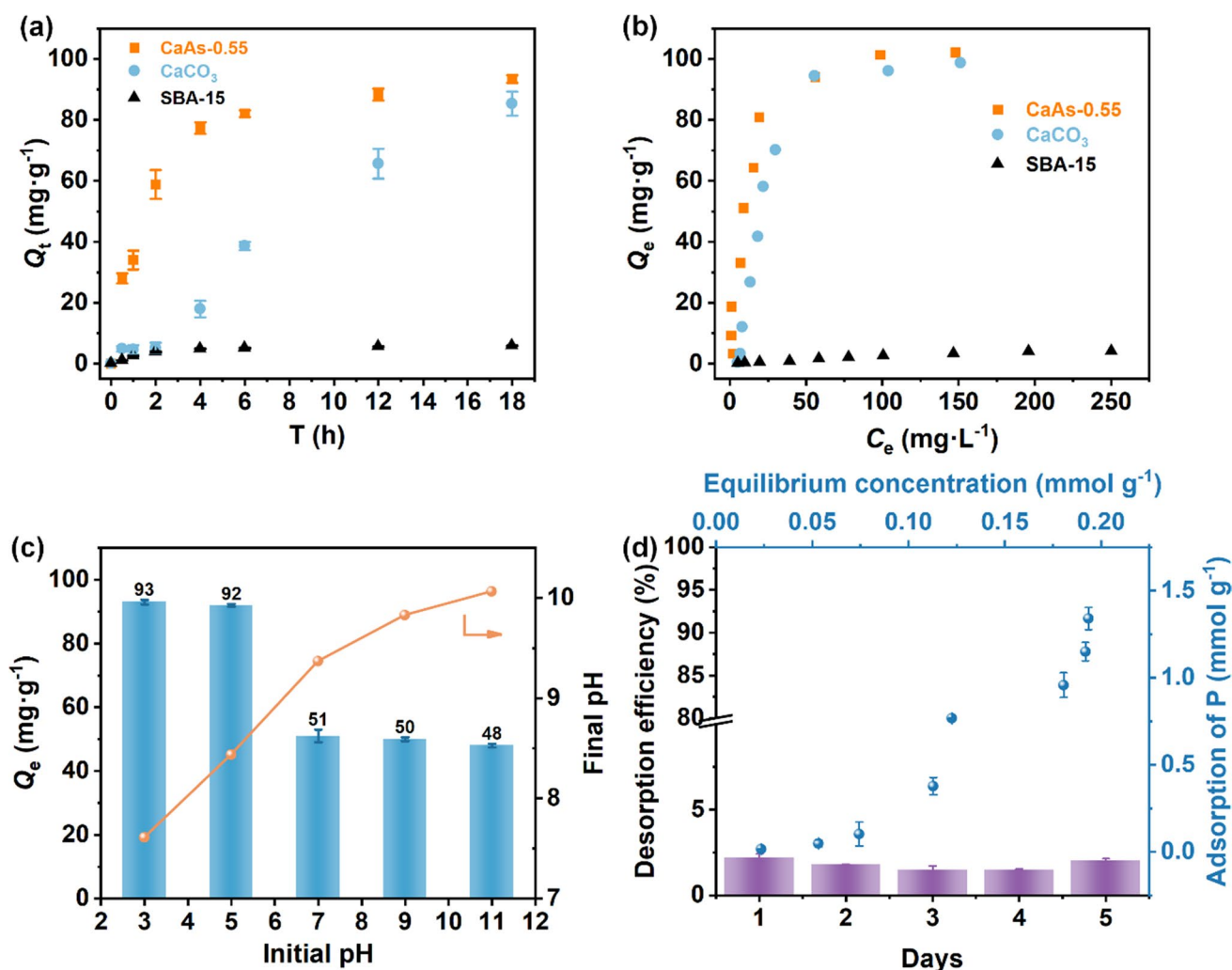

Fig. 7 Phosphate adsorption kinetics (**a**) and isotherms (**b**) of CaAS-0.55, pristine CaCO$_3$ and mesoporous SBA-15; effect of initial solution pH on phosphate adsorption on CaAs-0.55 (**c**), and pre-adsorption and desorption dynamics of phosphate on CaAS-0.55 in 10 mM NaCl at pH 7.0 (**d**)

CaCO$_3$ were compared and investigated. The adsorption capacities of CaAS-0.55 and CaCO$_3$ were remarkably improved with the increasing of initial phosphate concentration (Fig. 7b). The maximum adsorption capacity of phosphate on CaAS-0.55 and CaCO$_3$ reached 102.0 and 98.6 mg·g^{-1}. In contrast, the pure siliceous SBA-15 showed a weaker adsorption capacity of 3.9 mg·g^{-1} (Fig. 7b). This indicated that CaCO$_3$ nanoparticles is somehow the primary species that are beneficial for improving phosphate removal capability of the CaAS-0.55.

pH effect on phosphate adsorption of CaAS-0.55 material

Solution pH effect on phosphate adsorption performance of CaAS-0.55 was shown in Fig. 7c. The CaAS-0.55 material showed higher stronger adsorption capacity at lower pH. For example, the phosphate uptakes were about 92 mg·g^{-1} at pH values of 3−5, while that decreased to 51−48 mg·g^{-1} at pH 7−11 (Fig. 7c). Accordingly, the final pH increased after adsorption reactions reaching equilibrium, which was likely due to the formation of calcium phosphate (Xu et al. 2014a). The underlying mechanisms would be discussed later in details.

Desorption of phosphate on CaAS-0.55 material

Figure 7d illustrates the pre-adsorption isotherm and desorption dynamics of phosphate on the surface of CaAS-0.55 nanocomposite at pH 7.0. The phosphate uptake of CaAs-0.55 improved intensively from 0.62 to 41.5 mg·g^{-1} (0.020 to 1.337 mmol·g^{-1}) with increasing equilibrium concentration of phosphate from 0.024 to 0.194 mol·L^{-1}. Desorption dynamics results showed that the phosphate desorption from CaAs-0.55 surface relatively remained slightly around 2.21–1.50% at first 5 days, and even unchanged until the 13th day (Fig. 7d). This indicates that the phosphate adsorption on the surface of CaAS-0.55 was too strong to be released, since the chemisorption of phosphate was irreversible. Thus, the synthesized CaAS-0.55 showed great removal capacity to phosphate due to specific surface characteristics controlling the binding force change (Moharami and Jalali 2013).

Adsorption mechanisms

Modeling analysis

The adsorption kinetics of phosphate on CaAS-0.55 could be fitted well by the pseudo-first-order model ($R^2 > 0.990$) with k_1 constant of 0.53 h^{-1}, suggesting a fast adsorption rate at the initial reaction stage (Fig. 8a; Table 2). Moreover,
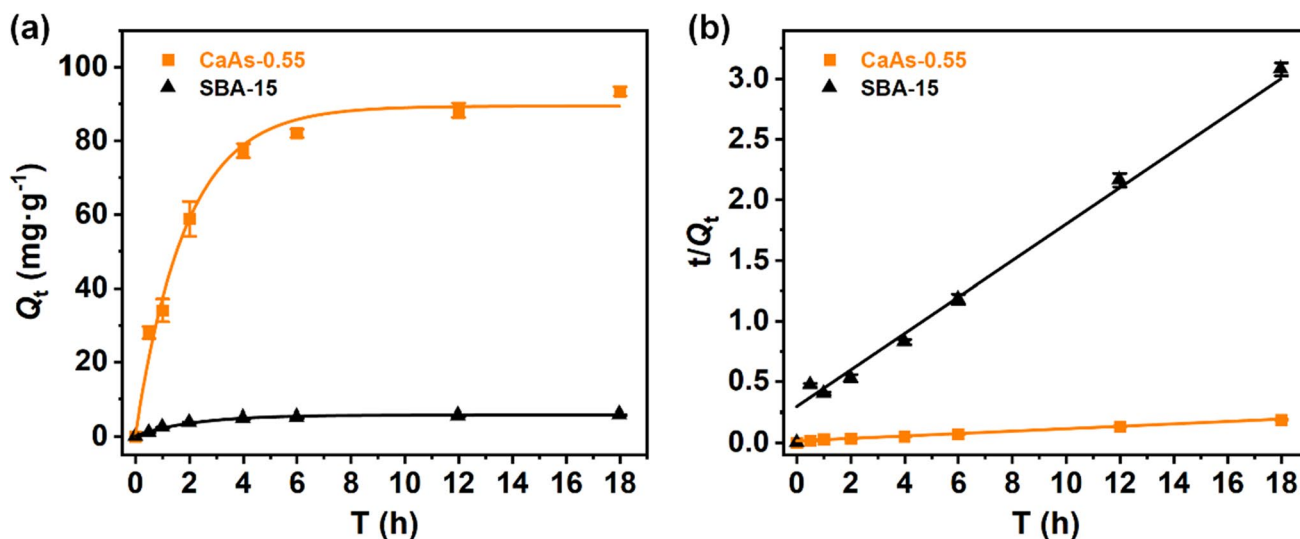

Fig. 8 Phosphate adsorption kinetics fitted by the pseudo-first-order model (**a**) and the pseudo-second-order model (**b**)

Table 2 Parameters obtained by fitting phosphate adsorption kinetics of materials using the pseudo-first-order and pseudo-second-order models

Samples	Pseudo-first-order model			Pseudo-second-order model		
	k_1 (h^{-1})	Q_e (mg·g^{-1})	R^2	k_2 (g·mg^{-1}·h^{-1})	Q_e (mg·g^{-1})	R^2
CaAs-0.55	0.53	89.30	0.99	0.007	100.61	0.99
SBA-15	0.47	5.74	0.98	0.067	6.76	0.98

the adsorption kinetics was also in accordance with the pseudo-second-order model ($R^2 > 0.99$), implying chemical adsorption played the dominant role in this adsorption system (Fig. 8a; Table 2). However, the adsorption kinetics of $CaCO_3$ failed to be fitted by both models, possibly because adsorption did not achieve equilibrium. Siliceous mesoporous SBA-15 showed a relatively slower phosphate removal rate with a pseudo-first-order k_1 constant of 0.47 h^{-1} and a pseudo-second-order k_2 constant of 0.067 $mg \cdot g^{-1} \cdot h^{-1}$ (Fig. 8a, b; Table 2), respectively.

Phosphate adsorption isotherms on CaAS-0.55, $CaCO_3$, and SBA-15 adsorbents were further analyzed by Langmuir and Freundlich equations. As shown in Table 3, Langmuir model showed a better fitting than Freundlich model due to the higher correlation coefficients of $R^2 > 0.97$. This implied that the adsorption amount of phosphate onto these materials slowly increased with the increase in initial concentration of phosphate, and then approached to the maximum value. Moreover, CaAS-0.55 had a maximum monolayer adsorption capacity of 114.21 $mg \cdot g^{-1}$ to phosphate, which was greatly stronger than 9.38 $mg \cdot g^{-1}$ monolayer adsorption capacity of SBA-15 (Table 3).

FT-IR analysis

FT-IR spectra of CaAS-x ($x = 0.1$–0.6) series in Fig. 9 showed that the characteristic peak of =Si-OH at 1079, 802, and 462 cm^{-1} remained unchanged after CaAS-x materials reacted with phosphate at pH 7.0, indicating the mesoporous SBA-15 as a support for $CaCO_3$ loading without reacting with phosphate. Note that the peaks at 1431, 874, and 713 cm^{-1} associated with C–O asymmetric stretching vibrations of carbonate (Ramola et al. 2021; Taweekarn et al. 2022) disappeared in Fig. 9, compared with FTIR of CaAS nanocomposites without phosphate as shown in Fig. 5. Instead, two new peaks at the wavelength of 565 cm^{-1} and 605 cm^{-1} were assigned to formation of SPO_4Ca (Wang et al. 2022a, b) (Fig. 9). This result indicated that the calcium carbonate on CaAS nanocomposites favors the effective chemisorption of phosphate and subsequently formation of phosphate calcium precipitation as the following equations (E.K. Gunawan et al.; Sø et al. 2011; Coreno-Alonso et al. 2014; Wang et al. 2021), which agreed with the exponential growth of phosphate adsorption on CaAS-0.55 as shown in Fig. 5b.
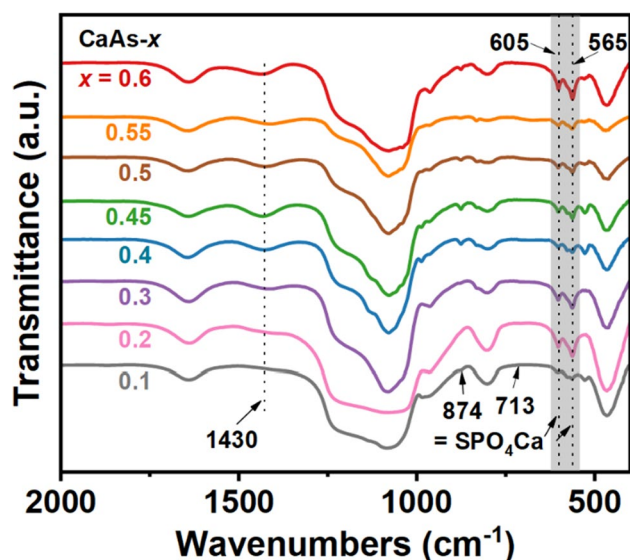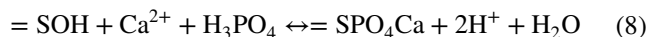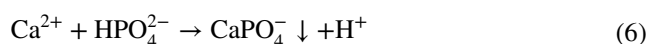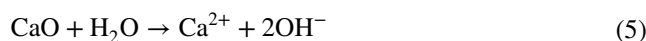

Fig. 9 FT-IR spectra of CaAS-x samples ($x = 0.1$–0.6) after reacting with 500 $mg \cdot L^{-1}$ phosphate at pH 7.0

$$CaO + H_2O \rightarrow Ca^{2+} + 2OH^- \tag{5}$$

$$Ca^{2+} + HPO_4^{2-} \rightarrow CaPO_4^- \downarrow + H^+ \tag{6}$$

$$2 = SOH + H_3PO_4 \leftrightarrow = S_2PO_4^- + H^+ + 2H_2O \tag{7}$$

$$= SOH + Ca^{2+} + H_3PO_4 \leftrightarrow = SPO_4Ca + 2H^+ + H_2O \tag{8}$$

$$= CaCO_3^- + HPO_4^{2-} \rightarrow = CaHPO_4 + CO_3^{2-} \tag{9}$$

$$= CaCO_3^- + CaPO_4^- \rightarrow = CaPO_4Ca^0 + CO_3^{2-} \tag{10}$$

where =SOH represents the active hydroxyl group bonded on the surface of adsorbent.

Additionally, with the increase in Ca/Si molar ratio for CaAS-x sample, these peaks at 565 cm^{-1} and 605 cm^{-1} wavenumbers became increasingly apparent, which suggested that increasing Ca/Si molar ratio (0.1–0.6) in CaAS-x increased the formation of phosphate calcium complexation in the mesoporous structure of CaAS-x promoting the phosphate removal efficiency (Fig. 6).

Table 3 Fitting parameters obtained by modeling phosphate adsorption isotherms of materials

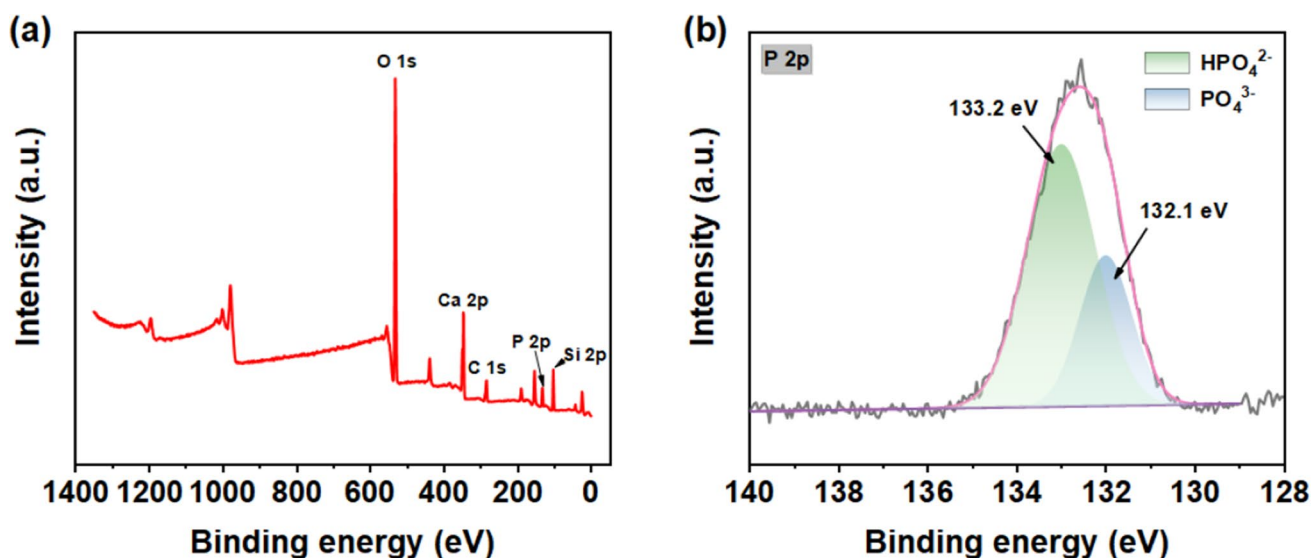| Samples	Langmuir model			Freundlich model		
	K_L (L·mg^{-1})	Q_{max} (mg·g^{-1})	R_L^2	K_F (mg·g^{-1}·(L·mg^{-1})$^{1/n}$)	$1/n_F$	R_F^2
CaAs-0.55	0.08	114.21	0.97	21.41	0.33	0.87
$CaCO_3$	0.07	108.36	0.97	9.18	0.50	0.90
SBA-15	0.003	9.38	0.98	0.06	0.75	0.97

Fig. 10 XPS full spectrum (**a**), and high resolution XPS spectra of P 2p for the CaAS-0.55 after reacting with phosphate (**b**)

XPS analysis

XPS analysis was conducted to further reveal the possible surface element composition and states on the CaAS nanocomposite (Fig. 10). After reacting with phosphate, the O, Ca, C, and Si elements of CaAS-0.55 showed in full XPS survey spectrum (Fig. 10a). Moreover, the two peaks of O–C=O at 133.2 and 132.1 eV appeared in P 2p spectra (Fig. 10b), which were assigned to $CaHPO_4$ and P=O (Huang et al. 2021; Wang et al. 2021). This could be again attributed to the formation of $=SPO_4Ca$, $=CaHPO_4^-$, and $=CaPO_4Ca^0$ complexation resulting from phosphate chemical adsorption on CaAS-0.55 as Eqs. 8–10. As shown in Fig. 7c, initial solution pH of 7.0 could increase up to about 9.5 as final pH after CaAS-0.55 reacted with phosphate, which was consistent with primary phosphate species as HPO_4^{2-} and PO_4^{3-} in solution during pH range of 7.5–12 (Du et al. 2022; Hasara et al. 2021).

For the high concentration of phosphate removal in wastewater, the challenge is to improve the phosphate adsorption capacity of adsorbents at natural pH since low pH favors phosphate adsorption. Accordingly, by application of CaAS nanocomposites designed as $CaCO_3$ incorporation in mesoporous SBA-15, the multiply growth of phosphate calcium precipitation fast occurrence on the surface of materials significantly improved the phosphate removal efficiency, especially in some sewage with high P concentration. The process conditions can possibly be further optimized by seeking to strike the appropriate balance between the costs and impacts incurred through an increased use of CaAS-*x* adsorbent and the environmental benefits of attaining low P in the water. In summary, this approach with an easy synthesis is environmental-friendly with high removal efficiency and is suitable for practical deployment.

Conclusions

In this research, a novel mesoporous CaAS-*x* nanocomposite was synthesized by loading $CaCO_3$ nanoparticles onto SBA-15 through a simple wet-impregnation method. First, by changing the molar ratio of Ca:Si (0.1–0.6) in the original solvent, the CaAS-*x* materials have been successfully obtained. When the increase of x as Ca/Si molar ratios from 0.1 to 0.6, CaAS-*x* series showed phosphate uptake percentage increased and then reached maximum. Also, the phosphate adsorption capacity and removal rate of CaAS nanocomposite raised up exponentially with the increase of phosphate concentration. This is because the mesoporous SBA-15 promotes the great disperse of $CaCO_3$ nanoparticles, leading to monolayer adsorption complexation formation of phosphate calcium, which is very stable and irreversible for desorption for long time period. Therefore, the proposed CaAS-0.55 composite might be a promising and efficient adsorbent with stable property for high concentration of phosphate removal from neutral contaminated wastewater.

Data availability The datasets used and/or analyzed during the current study are available from the corresponding author on reasonable request.

Declarations

Ethics approval and consent to participate Not applicable.

Consent for publication Not applicable.

Competing interests The authors declare no competing interests.

References

Akila GK, Chanaka MN, Sameera RG, Morgan C, Renel A, Dinesh M, Felio P, Charles UPJ, Todd M (2019) Fe$_3$O$_4$ nanoparticles dispersed on douglas fir biochar for phosphate sorption. ACS Appl Nano Mater 2:3467–3479

Almanassra IW, Kochkodan V, Ponnusamy G, Mckay G, Atieh MA, Al-Ansari T (2020) Carbide derived carbon (CDC) as novel adsorbent for ibuprofen removal from synthetic water and treated sewage effluent. J Environ Health Sci 18:1375–1390

Almanassra IW, Kochkodan V, Subeh M, Mckay G, Atieh M, Al-Ansari T (2020a) Phosphate removal from synthetic and treated sewage effluent by carbide derive carbon. J Water Process Eng 36:101323

Arslanolu H (2021) Production of low-cost adsorbent with small particle size from calcium carbonate rich residue carbonatation cake and their high performance phosphate adsorption applications. J Mater Res Technol 11(10):428–447

Berg U, Neumann T, Donnert D, Nüesch R, Stüben D (2004) Sediment capping in eutrophic lakes–efficiency of undisturbed calcite barriers to immobilize phosphorus. Appl Geochem 19(11):1759–1771

Chai Y, Wang L, Ren J, Dai WL (2015) A novel visible light-driven Ag$_3$PO$_4$/SBA-15 nanocomposite: preparation and application in the photo-degradation of pollutants. Appl Surf Sci 324:212–220

Chen J, Kong H, Wu D, Hu Z, Wang Z, Wang Y (2006) Removal of phosphate from aqueous solution by zeolite synthesized from fly ash. J Colloid Interf Sci 300(2):491–497

Chen X, Wang P, Xu J, Han Y, Jin H, Jin D, Peng X, Hong B, Li J, Yang Y, Ge H, Wang X (2017) Magnetic separation and adsorptive performance for methylene blue of mesoporous NiFe$_2$O$_4$/SBA-15 nanocomposites. Adv Powder Technol 28:2087–2093

Coreno-Alonso J, Coreno-Alonso O, Martínez-Rosales JM (2014) Apatite formation on alumina: the role of the initial adsorption of calcium and phosphate ions. Ceram Int 40(3):4909–4915

Cucarella V, Renman G (2009) Phosphorus sorption capacity of filter materials used for on-site wastewater treatment determined in batch experiments—a comparative study. J Environ Qual 38(2):381–392

Dan H, Ding Y, Wang E, Yang W, Zhu W (2020) Manganese dioxide-loaded mesoporous SBA-15 silica composites for effective removal of strontium from aqueous solution. Environ Res 191:110040

Du C, Xu N, Yao Z, Bai X, Gao Y, Peng L, Gu B, Zhao J (2022) Mechanistic insights into sulfate and phosphate mediated the dissolution of nano-zero-valent iron wrapped by tea polyphenols for hexavalent chromium removal. Sci Total Environ 850:157996

Gu MX, Kou Y, Qi SC, Shao MQ, Yue MB, Liu XQ, Sun LB (2019) Highly dispersive cobalt oxide constructed in confined space for oxygen evolution reaction. ACS Sustain Chem Eng 191:2837–2843

Gu SY, Wang YH, Zhang DF, Xiong MM, Gu H, Xu ZH (2022) Utilization of porous carbon synthesized with textile wastes via calcium

acetate template for tetracycline removal: The role of template agent and the formation mechanism. Chemosphere 289:133148

Hasara S, Abigail S, John E, Charles UP, Zhang XF, El BH, Rooban VKG, Thirumalai SW, Claudia R, Todd M (2021) Lignite, thermally-modified and Ca/Mg-modified lignite for phosphate remediation. Sci Total Environ 773:145631

House WA, Denison FH (2000) Factors influencing the measurements of equilibrium phosphate concentrations in river sediments. Water Res 34(4):1187–1200

Huang X, Yu L, Dong Y (2021) Corrosion resistance of a novel ceria doped aluminum phosphate ceramic coating on cast Al-Si alloy by steam-assisted curing. Corros Sci 182:109256

Karageorgiou K, Paschalis M, Anastassakis GN (2007) Removal of phosphate species from solution by adsorption onto calcite used as natural adsorbent. J Hazard Mater 139(3):447–452

Klibanski SB, Litor MI, Shenker M (2007) Overestimation of phosphorus adsorption capacity in reduced soils: an artifact of typical batch adsorption experiments. Soil Sci Soc Am J 71(4):1128–1136

Li J, Yang YT, Ge HL, Wang XQ (2017) Magnetic separation and adsorptive performance for methylene blue of mesoporous NiFe$_2$O$_4$/SBA-15 nanocomposites. Adv Powder Technol 28:2087–2093

Li MX, Liu JY, Xu YF, Qian GR (2016) Phosphate adsorption on metal oxides and metal hydroxides: a comparative review. Environ Rev 24(3):319–332

Liu FL, Xiang M, Wang AJ, Wang C, Hu BW (2021b) Efficient adsorption and reduction of Cr(VI) and U(VI) by nanoscale zero-valent iron supported on polydopamine-decorated SBA-15. Appl Surf Sci 568:150931

Liu HB, Chen TH, Zou XH, Xie QQ, Qing CS, Chen D et al (2013) Removal of phosphorus using nzvi derived from reducing natural goethite. Chem Eng J 234(12):80–87

Liu Y, Sheng X, Dong YH, Ma YJ (2012) Removal of high-concentration phosphate by calcite: effect of sulfate and pH. Desalination 289:66–71

Liu Y, Wang P, Gojenko B, Yu JJ, Wei LZ, Luo DG, Xiao TF (2021a) A review of water pollution arising from agriculture and mining activities in Central Asia: facts, causes and effects. Environ Pollut 291(15):118209

Mahmoudi F, Amini MM, Sillanpää M (2020) Hydrothermal synthesis of novel MIL-100(Fe)@SBA-15 composite material with high adsorption efficiency towards dye pollutants for wastewater remediation. J Taiwan Inst Chem E 116:303–313

Moharami S, Jalali M (2013) Removal of phosphorus from aqueous solution by Iranian natural adsorbents. Chem Eng J 223(1):328–339

Mudhoo A, Bhatnagar A, Rantalankila M, Srivastava V, Sillanpaa M (2019) Endosulfan removal through bioremediation, photocatalytic degradation, adsorption and membrane separation processes: A review. Chem Eng J 360:912–928

Nath SK, Dutta RK (2010a) Enhancement of limestone defluoridation of water by acetic and citric acids in fixed bed reactor. Clean Soil Air Water 38(7):614–622

Nath SK, Dutta RK (2010b) Fluoride removal from water using crushed limestone. Indian J Chem Techn 17:120–125

Peen CJ, Warren JG (2009) Investigating phosphorus sorption onto kaolinite using isothermal titration calorimetry. Soil Sci Soc Am J 73(2):560–568

Qiu H, Ye MC, Zhang MD, Zhang XL, Zhao Y, Yu JH (2021) Nano-hydroxyapatite encapsulated inside an anion exchanger for efficient defluoridation of neutral and weakly alkaline water. ACS EST Eng 1:46–54

Ramola S, Belwal T, Li CJ, Liu YX, Wang YY, Yang SM, Zhou CH (2021) Preparation and application of novel rice husk biochar–calcite composites for phosphate removal from aqueous medium. J Clean Prod 299(12):126802

Sø HU, Postma D, Jakobsen R, Larsen F (2011) Sorption of phosphate onto calcite; results from batch experiments and surface complexation modeling. Geochim Cosmochim Ac 75:2911–2933

Taweekarn T, Wongniramaikul W, Choodum A (2022) Removal and recovery of phosphate using a novel calcium silicate hydrate composite starch cryogel. J Environ Manage 301:113923

Vohla C, Koiv M, Bavor HJ, Chazarenc F, Mander U (2011) Filter materials for phosphorus removal from wastewater in treatment wetlands—a review. Ecol Eng 37:70–89

Wang F, Peng L, Xu N, Yao ZH, Li DP, Cheng XY (2021) Enhanced phosphate removal from solution using Al-doped aragonite nanoparticles. Colloid Surface A 630:127638–127647

Wang JZ, Ren C, Wang HT, Li W (2022a) Mechanisms of fluoride uptake by surface-modified calcite: a 19F solid-state NMR and TEM study. Chemosphere 294:133729

Wang WD, Wu XL, Ji JL, Xu S, Li DP, Lin Y, Chen ZG, Wu ZY, Sun LB (2022b) One-pot synthesis of Al-containing mesoporous silicas in a mildly acidic condition for efficient tetracycline adsorption. Micropor Mesopor Mat 346:112300

Wen ZP, Zhang YL, Dai CM (2014) Removal of phosphate from aqueous solution using nanoscale zerovalent iron (nZVI). Colloid Surface A 457(5):433–440

Wu ZY, Lu QY, Fu WH, Wang S, Liu CB, Xu N, Wang DT, Wang YM, Chen ZG (2014) Fabrication of mesoporous Al-SBA-15 as a methylene blue capturer via a spontaneous infiltration route. New J Chem 39(2):985–993

Wu ZY, Zhu W, Zhang M, Lin Y, Xu N, Chen F, Wang D, Chen Z (2018) Adsorption and synergetic Fenton-like degradation of methylene blue by a novel mesoporous α-Fe_2O_3/SiO_2 at neutral pH. Ind Eng Chem Res 57(16):5539–5549

Xing XW, Ren XM, Alharbi NS, Chen CL (2023) Efficient adsorption and reduction of Cr(VI) from aqueous solution by Santa Barbara Amorphous-15 (SBA-15) supported Fe/Ni bimetallic nanoparticles. J Colloid Interf Sci 629:744–754

Xu N, Li Y, Zheng L, Gao Y, Yin H, Zhao J, Chen Z, Chen J, Chen M (2014a) Synthesis and application of magnesium amorphous calcium carbonate for removal of high concentration of phosphate. Chem Eng J 251(1):102–110

Xu N, Yin H, Chen Z, Liu S, Chen M, Zhang J (2014b) Mechanisms of phosphate retention by calcite: effects of magnesium and pH. J Soil Sediment 14(3):495–503

Yao YL, Lu CY, Guan WS, Gou HG, Huang W (2014) Removal of phosphate species from solution by adsorption onto red and grey ceramic clay used as adsorbent. App Mech Mater 434:675–677

Zhang Q, Yu MH, Wang N, Qian JC, Gu Y, Du F, Lin Y, Chen F, Chen ZG, Wu ZY, Sun LB (2022) Porous Mn_2O_3/$p$$SiO_2$ nanocomposites on bio-scaffolds for tetracycline degradation. ACS App Nano Mater 5:9117–9128

Zhou JB, Yang SL, Yu JG (2011) Facile fabrication of mesoporous MgO microspheres and their enhanced adsorption performance for P from aqueous solutions. Colloid Surface A 379:102–108